Synthetic Antiferromagnetic Coupling Between Ultrathin Insulating Garnets

Juan M. Gomez-Perez,[1] Saül Vélez,[1,†] Lauren McKenzie-Sell,[2] Mario Amado,[2]
Javier Herrero-Martín,[3] Josu López-López,[1] S. Blanco-Canosa,[1,4] Luis E. Hueso,[1,4] Andrey Chuvilin,[1,4]
Jason W. A. Robinson,[2] and Fèlix Casanova[1,4,*]

[1]*CIC nanoGUNE, 20018, Donostia-San Sebastian, Basque Country, Spain*
[2]*Department of Materials Science and Metallurgy, University of Cambridge, 27 Charles Babbage Road,
Cambridge CB3 0FS, United Kingdom*
[3]*ALBA Synchrotron Light Source, Carrer de la Llum 2-26, 08290 Cerdanyola del Vallès, Catalonia, Spain*
[4]*IKERBASQUE, Basque Foundation for Science, 48013 Bilbao, Basque Country, Spain*

The use of magnetic insulators is attracting a lot of interest due to the rich variety of spin-dependent phenomena with potential applications for spintronic devices. Here, we report ultrathin yttrium iron garnet (YIG)/gadolinium iron garnet (GdIG) insulating bilayers on gadolinium gallium garnet (GGG). From spin Hall magnetoresistance (SMR) and x-ray magnetic circular dichroism measurements, we show that the YIG and GdIG magnetically couple antiparallel even in moderate in-plane magnetic fields. The results demonstrate an all-insulating equivalent of a synthetic antiferromagnet in a garnet-based thin film heterostructure and could open venues for insulators in magnetic devices. As an example, we demonstrate a memory element with orthogonal magnetization switching that can be read by SMR.

I. INTRODUCTION

Spintronics is an emerging field that involves the manipulation of not only electron charge, but also electron spin, and is seen as a promising alternative to conventional charge-based electronics. The application of magnetic insulators for spintronics is gaining interest because such materials offer advantages over metals such as long spin transmission lengths [1] and the absence of energy dissipation due to Ohmic losses [2]. Heavy metal (HM)/ferromagnetic insulator (FMI) heterostructures are an interesting platform where a plethora of spintronics phenomena has been discovered, including spin pumping [1,3,4], spin Hall magnetoresistance (SMR) [4,5], spin Seebeck effect [4,6], and many others [1,7–15]. SMR is based on the interaction between the spin-Hall-induced spin accumulation at the HM layer and the magnetization of the FMI at the HM/FMI interface [16]. SMR is thus a good candidate with which explore the magnetic properties of surfaces [17–19] because it is only sensitive to the first atomic planes of the FMI [20]. The most extensively used FMI in insulating spintronics is yttrium iron garnet or YIG ($Y_3Fe_5O_{12}$), due to its low Gilbert damping, soft ferrimagnetism, and negligible magnetic anisotropy [1,4–7,10–15,17,18,21–30]. Alternative magnetic insulators include

antiferromagnets [31–33], noncollinear magnets [34–36], hexagonal ferrites [8], ferrimagnetic spinels [19,37–39], and other ferrimagnetic garnets [9,40–45].

Downscaling is an important factor for spintronic devices, thus maintaining magnetic properties of the FMI at reduced dimensions is considered key for deterministic magnetization reversal due to spin-orbit torque [8,9] or for guiding magnons [2]. Since a top-down approach to nanofabrication requires the use of thin film materials, there is much effort focused on obtaining high quality YIG thin films. Standard growth techniques such as liquid phase epitaxy (LPE) are being pushed toward the 100-nm thickness [46], but sub-100-nm-thick films still require alternative techniques such as pulsed laser deposition (PLD) [47–49] or magnetron sputtering [50–53]. However, the material quality in these cases is not as consistently high that as seen in LPE-based YIG. For example, recent works report unusual magnetic anisotropy related to Fe^{3+} vacancies in PLD-grown YIG [47,48], and either exceptionally high magnetization [53] or a magnetization suppression [52] in sputtered films that could be related to the interface between YIG and the used substrate $Gd_3Ga_5O_{12}$ (GGG). The variety in the results and interpretations that can be found in the literature calls for an in-depth characterization of these thin YIG films.

In this paper, we report ultrathin (13-nm-thick) epitaxial YIG on GGG. Structural and compositional analysis by transmission electron microscopy (TEM)/scanning TEM (STEM) reveal a well-defined gadolinium iron garnet

---

*f.casanova@nanogune.eu
†Present address: Department of Materials, ETH Zürich, 8093 Zürich, Switzerland

(GdIG) interlayer at the YIG/GGG interface. The magnetic properties of the top YIG layer, characterized by SMR (using Pt as the spin-Hall material) and x-ray magnetic circular dichroism (XMCD) measurements, are dramatically modified with the YIG magnetization pinned antiparallel to the GdIG one. The results demonstrate the presence of a negative exchange interaction between YIG and GdIG that constitutes an insulating synthetic antiferromagnetic state, with a potential use in insulating spintronic devices [54]. For instance, we show that the complex interplay between the negative exchange interaction and the demagnetizing fields of the layers induce a memory effect that could be exploited as a device.

II. EXPERIMENTAL DETAILS

Epitaxial YIG (13-nm thick) is grown on (111)-oriented GGG by pulsed laser deposition (PLD) in an ultra-high vacuum chamber with a base pressure greater than 5×10^{-7} mbar. Prior to film growth, the GGG is rinsed with deionized water, acetone, and isopropyl alcohol and annealed *ex situ* in a constant flow of O_2 at 1000 °C for 8 h. The YIG is deposited using a KrF excimer laser (248-nm wavelength) with a nominal energy of 450 mJ and fluence of 2.2 W/cm². The films are grown under a stable atmosphere of 0.12 mbar of O_2 at 750 °C and a fixed frequency of 4 Hz for 20 min. An *in situ* postannealing at 850 °C is performed for 2 h in 0.5-mbar partial pressure of static O_2 and subsequently cooled down to room temperature at a rate of −5 °C/min. A 5-nm-thick Pt layer is magnetron-sputtered *ex situ* (80 W; 3 mtorr of Ar) and a Hall bar (width 450 nm, length 80 μm) is patterned by negative e-beam lithography and Ar-ion milling. Unpatterned samples for TEM/STEM and XMCD are capped with a 2-nm-thick layer of sputtered Pt.

TEM/STEM is performed on a Titan 60-300 electron microscope (FEI Co., The Netherlands) equipped with an EDAX detector (Ametek Inc., USA), high-angular annular dark-field (HAADF) STEM detector, and imaging Cs corrector. High-resolution TEM (HR TEM) images are obtained at 300 kV at negative Cs imaging conditions [55] so that atoms look bright. Composition profiles are acquired in STEM mode with drift correction utilizing an energy-dispersive x-ray spectroscopy (EDX) signal. Geometrical Phase Analysis (GPA) is performed on HR TEM images using all strong reflections for noise suppression [56]. Magnetotransport measurements are performed in a liquid-He cryostat (with a temperature T between 2 and 300 K, externally applied magnetic field H up to 9 T, and 360° sample rotation) using a current source ($I = 100$ μA) and a nanovoltmeter operating in the dc-reversal method [57–59]. XMCD measurements are performed across the Fe-$L_{2,3}$ absorption edges at the BL29-BOREAS beamline [60] of the ALBA Synchrotron Light Source (Barcelona, Spain), using surface-sensitive total electron yield (TEY) detection.

III. RESULTS AND DISCUSSION

A. Structural characterization

Figure 1 shows the structural and compositional analysis of a Pt/YIG film by TEM/STEM. Figure 1(a) shows a HR TEM cross-sectional micrograph where the top layer corresponds to Pt (polycrystalline), with epitaxial YIG on single-crystal GGG beneath. The YIG/GGG interface reveals an extended region with visually different contrast. Comparison of high-resolution contrast in the YIG, interfacial, and GGG regions [averaged unit cells are shown in the insets in Fig. 1(a)] show that within the same crystallographic structure there is a variation in distribution of heavy atoms from region to region. To confirm the nature of this middle region, we perform EDX analysis of a spatial distribution of the elements along the out-of-plane direction [see Fig. 1(b), the scan line is indicated in Fig. 1(a)]. From this analysis, we confirm that the film consists of 2-nm-thick Pt on the top surface, followed by a 12-nm-thick YIG layer that is Ga-doped. The interface between Pt and YIG is assumed to be atomically sharp, thus the inclination
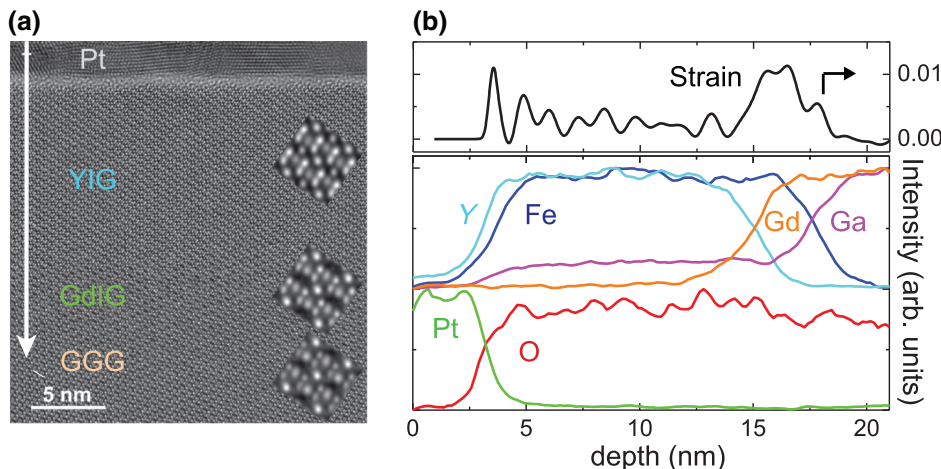

FIG. 1. (a) HR TEM micrograph of Pt (2 nm)/YIG (13 nm) (thicknesses are nominal) on GGG (111). Inset: averaged unit cells obtained in the different regions shown corresponding to YIG, GdIG, and GGG from top to bottom. (b) Spatial distribution of the elements extracted along the white arrow in (a) by spatially resolved EDX. The strain, extracted from the HR TEM image as a variation of the interplanar distance with respect to the GGG lattice, is also plotted as a black line. A strain of +0.01 means a lattice expansion by 1% in the out-of-plane direction.

of the Y curve and declination of the Pt curve give the estimation of spatial resolution of composition measurement, which is of the order of 1 nm. At the depth of 12 nm, Y concentration decreases to zero, though the slope of declination is lower than at the upper interface, indicating a smooth change of concentration in this case. Gd concentration in the same region increases complementarily to Y. At the same time, the decrease of Fe concentration is delayed by approximately 3 nm relative to Y, and Ga concentration changes complementarily to Fe. Thus, it may be concluded that, starting from a depth of 12 nm, Gd gradually (within a range of approximately 2 nm) substitutes Y in the lattice; similarly, Ga substitutes Fe but with an approximately 3-nm delay in depth. This delay results in the formation of a 2.8-nm-thick interlayer with a nominal composition corresponding to GdIG. The detailed analytical deconvolution of the concentration profiles gives a thickness of the "pure" GdIG as 2.2 nm [61].

Further insight into the nature of the layers can be obtained from the analysis of the interplanar distances in the direction normal to the surface. This is done by generalized GPA on the base of HR TEM images [56]. Variations of the interplanar distance are calculated in terms of strain with respect to the GGG lattice. The obtained strain profile is presented as a black line in Fig. 1(b) and shows that the region corresponding to GdIG composition is expanded by 1.1% with respect to GGG. This is lower than the 2.3% theoretically expected in epitaxial GdIG on GGG [62], which can be explained by the presence of an interdiffusion layer between GGG and GdIG that reduces the strain as compared to a sharp interface. The YIG layer shows an unexpected 0.2% expansion of the lattice (on average) with respect to GGG, in spite of the very similar lattice constant [62,63]. The out-of-plane expansion of the YIG lattice, which may be attributed to the presence of vacancies [47,48], is consistent with the x-ray diffraction measurements (0.35–0.6% expansion of the lattice) in the same deposition batch [61]. This detailed analysis confirms that we have a magnetic garnet bilayer. The presence of a Gd-doped YIG interlayer in YIG/GGG films after similar postannealing treatments has been recently reported [51,52], but in our case, we can confirm a well-defined, 2.2-nm-thick GdIG layer, and the fact that the YIG layer is Ga-doped.

B. Spin Hall magnetoresistance measurements

The ultrathin garnet bilayer can only be measured by standard magnetometry and ferromagnetic resonance at room temperature and with significant averaging, due to the weak moment compared to the paramagnetic substrate and small magnetic volume. At lower temperatures, both signals are reduced beyond detection [61].

A convenient alternative for magnetic characterization is the use of SMR, which is surface sensitive and does not depend on the magnetic volume. Therefore, we perform longitudinal-SMR measurements, which only probe the top surface magnetization [17–19] (the penetration depth of the conduction electrons into YIG is approximately 3–4 Å [20]) and thus the magnetization of the GdIG interlayer at the bottom interface is not expected to influence the SMR signal [52]. SMR depends on the relative angle of the surface magnetization in the FMI and the spin accumulation in the HM. When the spin accumulation and the magnetization are parallel (perpendicular) the longitudinal resistance state is low (high). A two-point measurement on the films confirmed that the YIG is insulating at room temperature [61,64]. The patterned Hall bar on the YIG (see Sec. II) corresponds to a Pt/YIG structure that has been widely measured before [5,17,21,22,24,30]. Figure 2 shows the longitudinal resistance R_L from a 4-point configuration at 2 K vs H applied along the three main axes of the sample [see Fig. 2(a)]. These field-dependent magnetoresistance (FDMR) curves are expected to show the
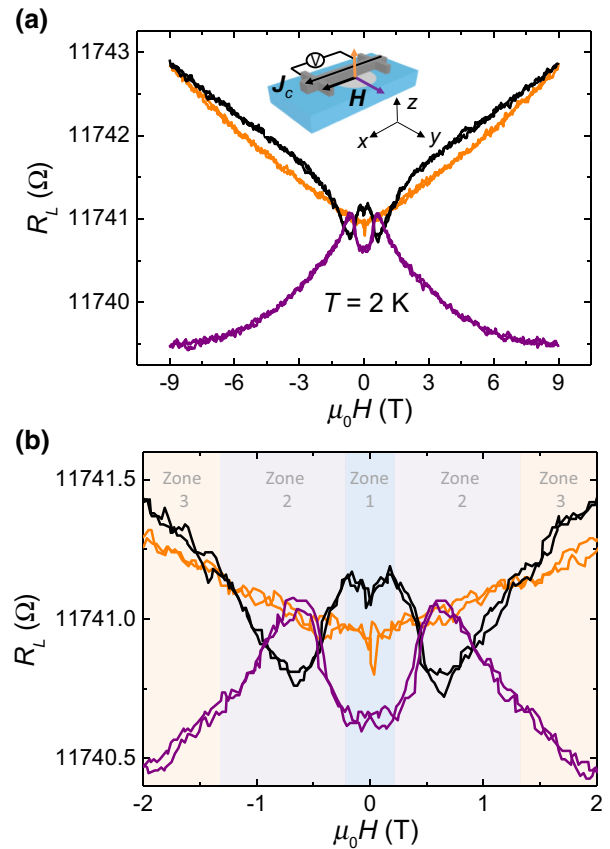

FIG. 2. (a) Longitudinal FDMR measurements at 2 K along the three main axes with a step size of 18 mT. Sketch indicates the definition of the axes, color code of the magnetic field direction, and the measurement configuration. (b) Zoom of the FDMR curves at low magnetic fields. Three different zones associated with the magnetization behavior are indicated (see text for details).

features of SMR: (i) a low resistance when the magnetic field saturates the magnetization in the y direction (i.e., parallel to the spin-Hall-induced spin accumulation in Pt) with a peak at low H corresponding to the magnetization reversal of the YIG film; and (ii) a high resistance value when H saturates the magnetization in the x or z direction (i.e., perpendicular to the spin accumulation in Pt) with a dip at low fields due to the magnetization reversal. However, the FDMR curves are very different from the ones observed so far in YIG [5,17,21,22]. A high $H \sim 8$ T is needed to saturate the magnetization of the film [see FDMR curve along the y direction in Fig. 2(a)], while YIG is expected to saturate within a few mT in-plane [22]. This result already suggests that the top surface magnetization of the 12-nm-thick YIG is strongly influenced by the 2.2-nm-thick GdIG at the bottom. Moreover, at relatively low H (below approximately 1.5 T) and at low temperature (below approximately 100 K, see Ref. [61] for high temperature behavior) the FDMR curves along the three main axes show unexpected crossings [see Fig. 2(b)], indicating complex magnetic behavior with the magnetization being noncollinear with the applied H. For detailed FDMR curves around zero field, see Ref. [61].

To better understand the magnetic properties and to confirm the noncollinear magnetization behavior of the bilayer, we perform angular-dependent magnetoresistance (ADMR) measurements in α, β and γ planes (see sketches in Fig. 3) at 2 K. The ADMR curves have three distinct behaviors depending on the applied H [zones 1–3 indicated in Fig. 2(b)]. At high H [above approximately 1.5 T, zone 3, Fig. 3(c)], we have a $\cos^2$ dependence

with the angle for α and β planes and no modulation for the γ plane, which is the expected dependence for SMR [16–19,38] when the magnetization is saturated and collinear with H. The same angular behavior is expected for Hanle magnetoresistance [22] (HMR), which has a common origin with SMR and is only relevant at very large fields. The absence of modulation in the γ plane rules out the presence of the magnetic proximity effect in our Pt layer [5]. At low H [below approximately 0.25 T, zone 1, Fig. 3(a)] we still have the $\cos^2$ dependence in the α plane, but the amplitude is smaller because the bilayer is not saturated [as evidenced in Fig. 2(a)]. However, we have an unusual ADMR for the β and γ planes. In the β plane, the ADMR curve does not follow a $\cos^2$ dependence, indicating that the magnetization and H are not collinear. When H is perfectly out-of-plane ($\beta = 0°$ and 180°), the magnetization also points out-of-plane. As soon as H rotates away from the out-of-plane into the y direction, the magnetization switches abruptly to the in-plane y direction ($\beta = 90°$ and 270°). This effect cannot be simply explained by the demagnetization field due to the strong shape anisotropy expected in the ultrathin film [65,66]. As we will see below, the presence of the GdIG layer also plays a role in this behavior. Accordingly, the same abrupt switching from the out-of-plane ($\gamma = 0°$ and 180°) into the in-plane x direction ($\gamma = 90°$ and 270°) when rotating H along the γ plane should not give any ADMR modulation; however, the dip in ADMR at $\gamma = 0°$ and 180° shows that a small net contribution of the magnetization along y exists, probably because the YIG film breaks into domains.
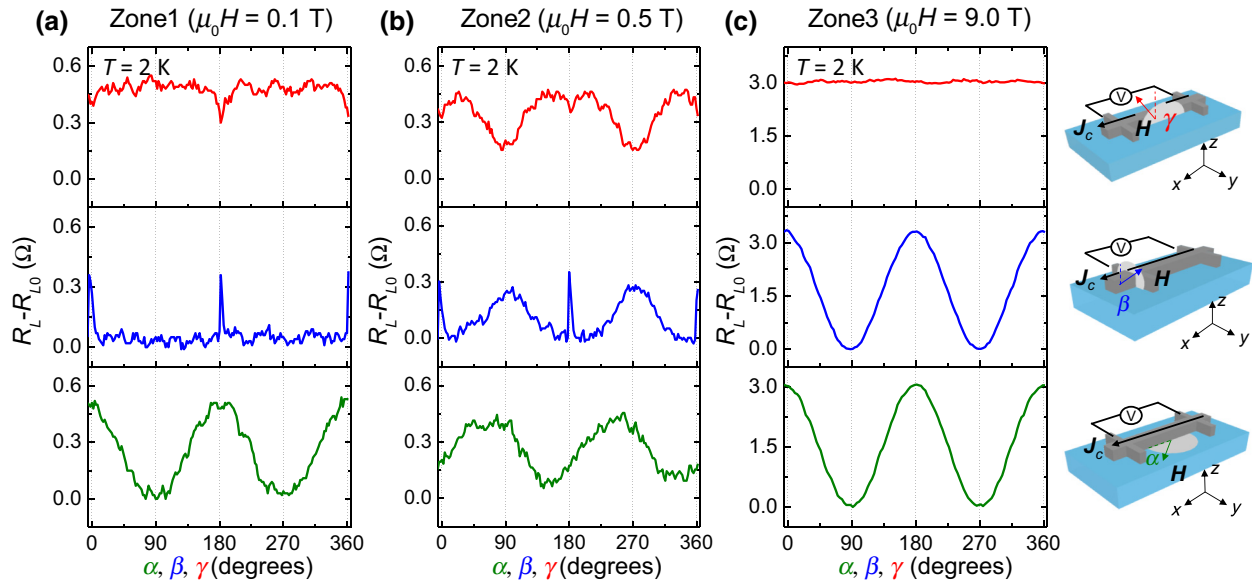

FIG. 3.   Longitudinal ADMR measurements at 2 K along the three relevant H-rotation planes (α, β, γ) for different applied magnetic fields: (a) 0.1 T (zone 1), (b) 0.5 T (zone 2), and (c) 9 T (zone 3). A different background R_{L0} is subtracted for the ADMR curves at each field. Sketches indicate the definitions of the angles, the axes, and the measurement configuration. Dotted line at each sketch corresponds to 0°.

At intermediate magnetic fields [0.25 T $\leq H \leq$ 1.5 T, zone 2, Fig. 3(b)], we can see that the ADMR curve for the α plane maintains the $\cos^2$ dependence, but with a phase shift α_0 (which can be either approximately 112° or approximately 68° for the example at $H = 0.5$ T shown here). This α_0 should correspond to the angle between H and the surface magnetization. This is confirmed by an extra modulation in the ADMR curves for the β and γ planes. Two broad peaks appear, with a maximum in the β scan when the magnetization is in-plane ($\beta = 90°$ and 270°) and a minimum in the γ scan when the magnetization is in-plane ($\gamma = 90°$ and 270°). This result is equivalent to the observed behavior in the α plane (note that the magnetic field direction at $\beta = 90°$ in the β scan is the same as $\alpha = 90°$ in the α scan and the magnetic field direction at $\gamma = 90°$ is the same as $\alpha = 0°$, see sketches in Fig. 3). When the phase shift for the α scan occurs in zone 2, the ADMR value at $\alpha = 90°$ increases and the value at $\alpha = 0°$ decreases. This very same effect shows up in the β scan with a relative maximum (ADMR value increases) developing at $\beta = 90°$ and in the γ scan with a relative minimum (ADMR value decreases) developing at $\gamma = 90°$.

To study with more detail the behavior of α_0, we perform ADMR measurements in the α plane for different applied magnetic fields (from 20 mT to 2 T). Figure 4(a) shows how the phase of the ADMR curves shift with increasing H (for the amplitude of the ADMR as a function of H, see Ref. [61]). Figure 4(b) plots α_0 as a function of H, showing a monotonic change between 0° and 180°. Although we cannot, in principle, determine if the phase shift at low fields corresponds to 0° or 180°, we assume that α_0 goes from 180° at low fields to 0° at high fields because this is physically more plausible. The three different zones already described can be distinguished in this plot: (i) zone 1, where the surface magnetization is antiparallel to the applied H; (ii) zone 2, where the surface magnetization has a certain angle with H; and (iii) zone

3, where the surface magnetization is almost aligned with H. Note that with the SMR symmetry, we cannot determine whether the rotation occurs clockwise [angle between surface magnetization and H equal to α_0, as assumed in Fig. 4(b)] or counterclockwise (angle between surface magnetization and H equal to 360° α_0).

C. X-ray magnetic circular dichroism measurements

To confirm this unconventional behavior that suggests that the surface magnetization of YIG opposes a low external field and only aligns parallel under a high enough field (>1.5 T), we perform XMCD, a technique that extracts information of the magnetization associated with each atomic species. The sample is oriented with its surface forming a grazing angle with respect to the propagation direction of incident x-rays (in-plane configuration), H is applied parallel to the x-ray beam, and TEY detection is used, which is sensitive to the surface (up to 2–3-nm depth) [67]. We obtain the typical XMCD spectrum for standard YIG at Fe $L_{2,3}$ absorption edges [61]. From these data and applying the sum rules for XMCD spectra at different H values, we can estimate the magnetization per Fe ion and plot the hysteresis loop [see Fig. 4(c)]. The loop clearly confirms our scenario: a negative net magnetization is measured at low applied H, i.e., the magnetization vector of the YIG surface is aligned antiparallel to H. The net magnetization is reduced with increasing H because the magnetization vector starts rotating monotonously toward the applied H and, at a certain value of H, becomes perpendicular to H, leading to no net magnetization. At higher H, the net magnetization becomes positive while the magnetization vector approaches a collinear configuration with H, finally saturating at very high fields. Note that the saturation magnetization (3–3.5 μ_B/Fe) is lower than expected in YIG (5 μ_B/Fe), which can be explained by the presence of Ga substituting Fe along our YIG film [68]. With

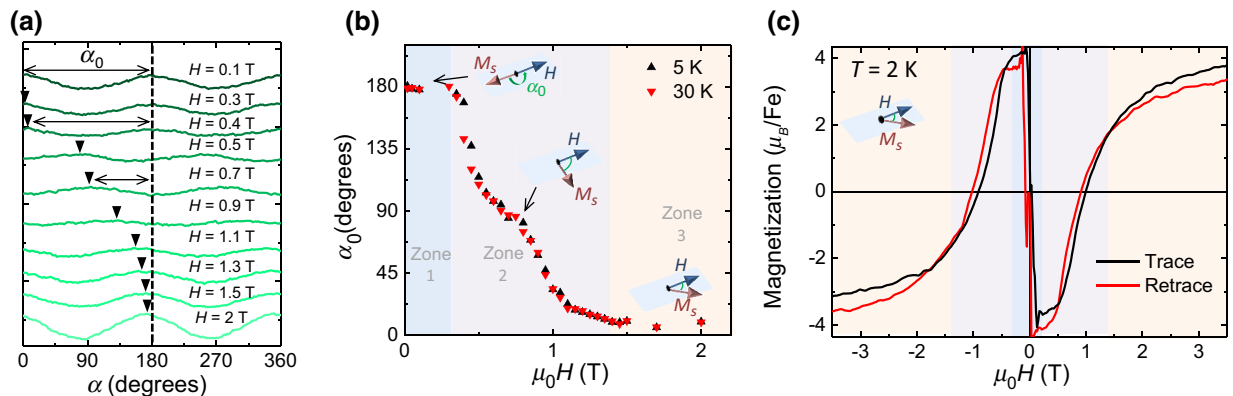FIG. 4. (a) Longitudinal ADMR measurements for different applied magnetic fields in the α plane at 5 K. (b) Phase shift (α_0) as a function of magnetic field taken from data in (a). α_0 corresponds to the effective angle between the magnetization vector and the applied magnetic field. (c) Hysteresis loop measured by XMCD with the magnetic field applied in-plane at 2 K.

a particular configuration of the XMCD measurements that is sensitive to the magnetization perpendicular to the applied field, we can clarify whether the surface magnetization is rotating counterclockwise or clockwise when increasing the magnetic field (see Ref. [61]).

The behavior of the surface magnetization of YIG observed both via SMR and XMCD can be explained if we consider that YIG is in fact coupled antiparallel to the GdIG interlayer. A hysteresis loop similar to the one in Fig. 4(c) has been recently observed in Ni/Gd layers and attributed to the negative exchange coupling between the transition metal and rare-earth ferromagnets [69]. YIG has two magnetic sublattices [3 tetrahedrally coordinated ("FeD") and 2 octahedrally coordinated ("FeA") Fe^{3+} ions per formula unit] which are antiferromagnetically coupled ($J_{ad} \sim 32$ cm^{-1}) [70], leading to its ferrimagnetism, with the magnetization dominated by the FeD sublattice. GdIG has the same iron-garnet-crystal structure, with a third magnetic sublattice (3 dodecahedrally coordinated Gd^{3+} ions per formula unit), which is ferromagnetically coupled to the FeA sublattice ($J_{ac} \sim 1.75$ cm^{-1}) and antiferromagnetically coupled to the FeD sublattice ($J_{cd} \sim 7$ cm^{-1}) [70]. The strong variation of the magnetization of the Gd sublattice with temperature makes GdIG a compensated ferrimagnet, with the magnetization dominated by the Gd and FeA sublattices below room temperature [43,45,71]. We hypothesize that the perfect epitaxy of the crystal structure at the YIG/GdIG interface [Fig. 1(a)] will favor the continuity of the FeA and FeD sublattices across the interface. Such continuity leads to an antiferromagnetic coupling between the net magnetization of the GdIG (dominated by Gd) and the net magnetization of the YIG (dominated by FeD), which should have the energy of J_{cd} (approximately 0.14 meV). This very same coupling has been deduced from recent magneto-optical spectroscopy [51] and polarized neutron reflectivity [52] experiments in YIG/GGG interfaces. In our case, the Gd magnetization at low T is so high that a 2.2-nm-thick GdIG layer can pin the whole 12-nm-thick YIG layer antiparallel to H.

We are probing only the top surface magnetization by SMR and XMCD, whereas the different boundary conditions lead to different magnetic states at the top and the bottom interfaces. The complete qualitative picture (see Ref. [61]) of the magnetic state based on the experimental evidence discussed above would be as follows: the magnetization at the bottom interface of YIG film is strongly antiferromagnetically coupled to the magnetization of the GdIG [45,72]. At zero field, the top surface magnetization of YIG is antiparallel to the magnetic field (as observed from SMR and XMCD measurements). This would be the only situation where the magnetization at the top and bottom interfaces have the same orientation, leading to a uniform magnetization along the YIG film. When applying a moderate field, the top surface magnetization coherently rotates (as observed from SMR

and XMCD measurements). Since moderate fields cannot break the strong antiferromagnetic coupling between Gd moments and FeD moments at the YIG/GdIG interface (the magnetic field needed to break such coupling would be hundreds of teslas, see Ref. [43]), the bottom surface magnetization would be pinned. These two different boundary conditions would lead to a helical magnetization from top to bottom. Above approximately 1.5 T, the top surface magnetization is mostly aligned with the field, and the helical structure remains. Further increasing the magnetic field favors the parallel alignment of the YIG magnetization, but the antiparallel pinning at the bottom YIG surface will prevent a complete uniform magnetization along the film even at the largest applied field. This behavior of the magnetization profile is similar to the one reported in Gd/Ni multilayers, also dominated by antiferromagnetic coupling at the interfaces [69]. The behavior of our bilayer is thus equivalent to that of a synthetic antiferromagnet [73], although we are not aware of previous reports of such a man-made system with insulating materials.

D. Memory effect

The presence of the negative exchange coupling between YIG and GdIG will also explain the sharp switching from the out-of-plane to in-plane magnetization deduced from the shape of the ADMR in the β plane [Figs. 3(a) and 3(b)]. The strong and opposing demagnetization fields expected from the YIG and GdIG layers combined with the antiferromagnetic coupling between them will favor the switching of the entire bilayer magnetization to the plane, much sharper than the case of a single YIG layer of similar thickness [65]. This effect is confirmed with detailed FDMR measurements sweeping at low magnetic fields along the z direction (Fig. 5): the higher resistance state corresponds to the YIG magnetization pointing out-of-plane and the lower resistance state around zero
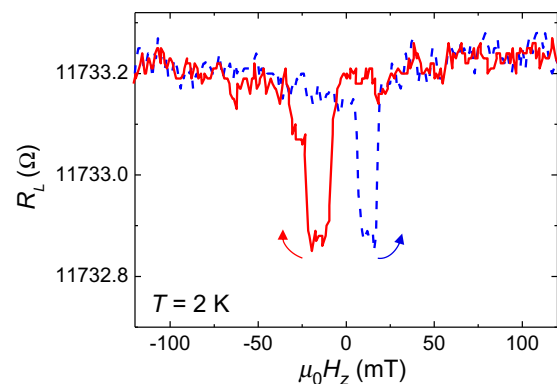

FIG. 5.   Longitudinal FDMR measurement (trace and retrace) at 2 K with the magnetic field applied along the z direction (out-of-plane).

field corresponds to in-plane magnetization. Interestingly, the switching has a clear hysteretic behavior, which is probably due to the complex interplay between antiparallel coupling and the opposing demagnetizing fields of each layer. Switching between two metastable states with orthogonal magnetic configurations can be used in a memory device which is written with a very low magnetic field and read by longitudinal SMR. This will be an advantage with respect to previous proposals of a memory device based on magnetic insulators with perpendicular magnetic anisotropy, because they use the transverse SMR to read the magnetization state, which has a resistance change almost three orders of magnitude smaller [8,9].

IV. CONCLUSIONS

We structurally and magnetically characterize ultrathin epitaxial YIG films on GGG, which reveal an atomically well-defined interlayer of GdIG at the YIG/GGG interface. From SMR and XMCD, we demonstrate that the YIG magnetization opposes moderate external magnetic fields. This unconventional behavior occurs because YIG/GdIG magnetically couple antiparallel, forming the equivalent to a synthetic antiferromagnet with the exceptional fact of being insulating. Furthermore, we observe a memory effect between orthogonal magnetization orientations, which can be read with an adjacent Pt film via longitudinal SMR measurements. This bilayer system can be further engineered to optimize the functionalities exploited in insulating spintronic devices, such as writing operations with spin-orbit torque and reading operations with SMR in insulating magnetic memories [8,9], or in devices where the application of antiferromagnets [74] and their synthetic versions [54] is advantageous.

[1] Y. Kajiwara, K. Harii, S. Takahashi, J. Ohe, K. Uchida, M. Mizuguchi, H. Umezawa, H. Kawai, K. Ando, K. Takanashi, S. Maekawa, and E. Saitoh, Transmission of electrical signals by spin-wave interconversion in a magnetic insulator, Nature **464**, 262 (2010).

[2] A. V. Chumak, V. I. Vasyuchka, A. A. Serga, and B. Hillebrands, Magnon spintronics, Nat. Phys. **11**, 453 (2015).

[3] E. Saitoh, M. Ueda, H. Miyajima, and G. Tatara, Conversion of spin current into charge current at room temperature: Inverse spin-Hall effect, Appl. Phys. Lett. **88**, 182509 (2006).

[4] M. Weiler, M. Althammer, M. Schreier, J. Lotze, M. Pernpeintner, S. Meyer, H. Huebl, R. Gross, A. Kamra, J. Xiao, Y. T. Chen, H. Jiao, G. E. W. Bauer, and S. T. B. Goennenwein, Experimental Test of the Spin Mixing Interface Conductivity Concept, Phys. Rev. Lett. **111**, 176601 (2013).

[5] H. Nakayama, M. Althammer, Y. T. Chen, K. Uchida, Y. Kajiwara, D. Kikuchi, T. Ohtani, S. Geprägs, M. Opel, S. Takahashi, R. Gross, G. E. W. Bauer, S. T. B. Goennenwein, and E. Saitoh, Spin Hall Magnetoresistance Induced by a Nonequilibrium Proximity Effect, Phys. Rev. Lett. **110**, 206601 (2013).

[6] K. Uchida, J. Xiao, H. Adachi, J. Ohe, S. Takahashi, J. Ieda, T. Ota, Y. Kajiwara, H. Umezawa, H. Kawai, G. E. W. Bauer, S. Maekawa, and E. Saitoh, Spin Seebeck insulator, Nat. Mater. **9**, 894 (2010).

[7] J. Flipse, F. K. Dejene, D. Wagenaar, G. E. W. Bauer, J. Ben Youssef, and B. J. Van Wees, Observation of the Spin Peltier Effect for Magnetic Insulators, Phys. Rev. Lett. **113**, 027601 (2014).

[8] P. Li, T. Liu, H. Chang, A. Kalitsov, W. Zhang, G. Csaba, W. Li, D. Richardson, A. DeMann, G. Rimal, H. Dey, J. S. Jiang, W. Porod, S. B. Field, J. Tang, M. C. Marconi, A. Hoffmann, O. Mryasov, and M. Wu, Spin–orbit torque-assisted switching in magnetic insulator thin films with perpendicular magnetic anisotropy, Nat. Commun. **7**, 12688 (2016).

[9] C. O. Avci, A. Quindeau, C.-F. Pai, M. Mann, L. Caretta, A. S. Tang, M. C. Onbasli, C. A. Ross, and G. S. D. Beach, Current-induced switching in a magnetic insulator, Nat. Mater. **16**, 309 (2016).

[10] E. Villamor, M. Isasa, S. Vélez, A. Bedoya-Pinto, P. Vavassori, L. E. Hueso, F. S. Bergeret, and F. Casanova, Modulation of pure spin currents with a ferromagnetic insulator, Phys. Rev. B **91**, 020403(R) (2015).

[11] F. K. Dejene, N. Vlietstra, D. Luc, X. Waintal, J. Ben Youssef, and B. J. Van Wees, Control of spin current by a magnetic YIG substrate in NiFe/Al nonlocal spin valves, Phys. Rev. B **91**, 100404(R) (2015).

[12] S. Singh, J. Katoch, T. Zhu, K. Y. Meng, T. Liu, J. T. Brangham, F. Yang, M. E. Flatté, and R. K. Kawakami, Strong Modulation of Spin Currents in Bilayer Graphene by Static and Fluctuating Proximity Exchange Fields, Phys. Rev. Lett. **118**, 187201 (2017).

[13] S. Meyer, Y.-T. Chen, S. Wimmer, M. Althammer, S. Geprägs, H. Huebl, D. Ködderitzsch, H. Ebert, G. E. W. Bauer, R. Gross, and S. T. B. Goennenwein, Observation of the spin Nernst effect, Nat. Mater. **16**, 977 (2017).

[14] D. Ellsworth, L. Lu, J. Lan, H. Chang, P. Li, Z. Wang, J. Hu, B. Johnson, Y. Bian, J. Xiao, R. Wu, and M. Wu, Photo-spin-voltaic effect, Nat. Phys. **12**, 861 (2016).

[15] L. J. Cornelissen, J. Liu, R. A. Duine, J. Ben Youssef, and B. J. Van Wees, Long distance transport of magnon spin information in a magnetic insulator at room temperature, Nat. Phys. **11**, 1022 (2015).

[16] Y.-T. Chen, S. Takahashi, H. Nakayama, M. Althammer, S. Goennenwein, E. Saitoh, and G. E. W. Bauer, Theory of spin Hall magnetoresistance, Phys. Rev. B **87**, 144411 (2013).

[17] S. Vélez, A. Bedoya-Pinto, W. Yan, L. E. Hueso, and F. Casanova, Competing effects at Pt/YIG interfaces: Spin Hall magnetoresistance, magnon excitations, and magnetic frustration, Phys. Rev. B **94**, 174405 (2016).

[18] D. Hou, Z. Qiu, J. Barker, K. Sato, K. Yamamoto, S. Vélez, J. M. Gomez-Perez, L. E. Hueso, F. Casanova, and E. Saitoh, Tunable Sign Change of Spin Hall Magnetoresistance in Pt/NiO/YIG Structures, Phys. Rev. Lett. **118**, 147202 (2017).

[19] M. Isasa, S. Vélez, E. Sagasta, A. Bedoya-Pinto, N. Dix, F. Sánchez, L. E. Hueso, J. Fontcuberta, and F. Casanova, Spin Hall Magnetoresistance as a Probe for Surface Magnetization in Pt/CoFe$_2$O$_4$ Bilayers, Phys. Rev. Appl. **6**, 034007 (2016).

[20] X. Jia, K. Liu, K. Xia, and G. E. W. Bauer, Spin transfer torque on magnetic insulators, EPL (Europhys. Lett.) **96**, 17005 (2011).

[21] N. Vlietstra, J. Shan, V. Castel, B. J. Van Wees, and J. Ben Youssef, Spin-Hall magnetoresistance in platinum on yttrium iron garnet: Dependence on platinum thickness and in-plane/out-of-plane magnetization, Phys. Rev. B **87**, 184421 (2013).

[22] S. Vélez, V. N. Golovach, A. Bedoya-Pinto, M. Isasa, E. Sagasta, M. Abadia, C. Rogero, L. E. Hueso, F. S. Bergeret, and F. Casanova, Hanle Magnetoresistance in Thin Metal Films with Strong Spin-Orbit Coupling, Phys. Rev. Lett. **116**, 016603 (2016).

[23] J. Shan, L. J. Cornelissen, N. Vlietstra, J. Ben Youssef, T. Kuschel, R. A. Duine, and B. J. Van Wees, Influence of yttrium iron garnet thickness and heater opacity on the nonlocal transport of electrically and thermally excited magnons, Phys. Rev. B **94**, 174437 (2016).

[24] S. T. B. Goennenwein, R. Schlitz, M. Pernpeintner, K. Ganzhorn, M. Althammer, R. Gross, and H. Huebl, Non-local magnetoresistance in YIG/Pt nanostructures, Appl. Phys. Lett. **107**, 172405 (2015).

[25] B. L. Giles, Z. Yang, J. S. Jamison, and R. C. Myers, Long-range pure magnon spin diffusion observed in a nonlocal spin-Seebeck geometry, Phys. Rev. B **92**, 224415 (2015).

[26] B. L. Giles, Z. Yang, J. Jamison, J. M. Gomez-perez, S. Vélez, E. Luis, F. Casanova, and R. C. Myers, Thermally driven long range magnon spin currents in yttrium iron garnet due to intrinsic spin Seebeck effect, Phys. Rev. B **96**, 180412(R) (2017).

[27] K. Ganzhorn, S. Klingler, T. Wimmer, S. Geprägs, R. Gross, H. Huebl, and S. T. B. Goennenwein, Magnon-based

logic in a multi-terminal YIG/Pt nanostructure, Appl. Phys. Lett. **109**, 022405 (2016).

[28] L. J. Cornelissen, J. Shan, and B. J. Van Wees, Temperature dependence of the magnon spin diffusion length and magnon spin conductivity in the magnetic insulator yttrium iron garnet, Phys. Rev. B **94**, 180402(R) (2016).

[29] L. J. Cornelissen and B. J. Van Wees, Magnetic field dependence of the magnon spin diffusion length in the magnetic insulator yttrium iron garnet, Phys. Rev. B **93**, 020403(R) (2016).

[30] N. Vlietstra, J. Shan, V. Castel, J. Ben Youssef, G. E. W. Bauer, and B. J. Van Wees, Exchange magnetic field torques in YIG/Pt bilayers observed by the spin-Hall magnetoresistance, Appl. Phys. Lett. **103**, 032401 (2013).

[31] G. R. Hoogeboom, A. Aqeel, T. Kuschel, T. T. M. Palstra, and B. J. Van Wees, Negative spin Hall magnetoresistance of Pt on the bulk easy-plane antiferromagnet NiO, Appl. Phys. Lett. **111**, 052409 (2017).

[32] L. Baldrati, A. Ross, T. Niizeki, C. Schneider, R. Ramos, J. Cramer, O. Gomonay, M. Filianina, T. Savchenko, D. Heinze, A. Kleibert, E. Saitoh, J. Sinova, and M. Kläui, Full angular dependence of the spin Hall and ordinary magnetoresistance in epitaxial antiferromagnetic NiO(001)/Pt thin films, Phys. Rev. B **98**, 024422 (2018).

[33] Y. Ji, J. Miao, K. K. Meng, Z. Y. Ren, B. W. Dong, X. G. Xu, Y. Wu, and Y. Jiang, Spin Hall magnetoresistance in an antiferromagnetic magnetoelectric Cr$_2$O$_3$/heavy-metal W heterostructure, Appl. Phys. Lett. **110**, 262401 (2017).

[34] A. Aqeel, N. Vlietstra, A. Roy, M. Mostovoy, B. J. Van Wees, and T. T. M. Palstra, Electrical detection of spiral spin structures in Pt|Cu$_2$OSeO$_3$ heterostructures, Phys. Rev. B **94**, 134418 (2016).

[35] A. Aqeel, N. Vlietstra, J. A. Heuver, G. E. W. Bauer, B. Noheda, B. J. Van Wees, and T. T. M. Palstra, Spin-Hall magnetoresistance and spin Seebeck effect in spin-spiral and paramagnetic phases of multiferroic CoCr$_2$O$_4$ films, Phys. Rev. B **92**, 224410 (2015).

[36] F. Jonietz, S. Mulbauer, C. Pfleiderer, A. Neubauer, W. Munzer, A. Bauer, T. Adams, R. Georgii, P. Boni, R. A. Duine, K. Everschor, M. Garst, and A. Rosch, Spin transfer torques in MnSi, Science (80-.) **330**, 1648 (2011).

[37] M. Valvidares, N. Dix, M. Isasa, K. Ollefs, F. Wilhelm, A. Rogalev, F. Sánchez, E. Pellegrin, A. Bedoya-Pinto, P. Gargiani, L. E. Hueso, F. Casanova, and J. Fontcuberta, Absence of magnetic proximity effects in magnetoresistive Pt/CoFe$_2$O$_4$ hybrid interfaces, Phys. Rev. B **93**, 214415 (2016).

[38] M. Isasa, A. Bedoya-Pinto, S. Vélez, F. Golmar, F. Sánchez, L. E. Hueso, J. Fontcuberta, and F. Casanova, Spin Hall magnetoresistance at Pt/CoFe$_2$O$_4$ interfaces and texture effects, Appl. Phys. Lett. **105**, 142402 (2014).

[39] J. Shan, P. Bougiatioti, L. Liang, G. Reiss, T. Kuschel, and B. J. van Wees, Nonlocal magnon spin transport in NiFe$_2$O$_4$ thin films, Appl. Phys. Lett. **110**, 132406 (2017).

[40] H. Maier-Flaig, M. Harder, S. Klingler, Z. Qiu, E. Saitoh, M. Weiler, S. Geprägs, R. Gross, S. T. B. Goennenwein, and H. Huebl, Tunable magnon-photon coupling in a compensating ferrimagnet - from weak to strong coupling, Appl. Phys. Lett. **110**, 132401 (2017).

[41] J. Cramer, E. J. Guo, S. Geprägs, A. Kehlberger, Y. P. Ivanov, K. Ganzhorn, F. Della Coletta, M. Althammer,

H. Huebl, R. Gross, J. Kosel, M. Kläui, and S. T. B. Goennenwein, Magnon mode selective spin transport in compensated ferrimagnets, Nano Lett. **17**, 3334 (2017).

[42] K. Ganzhorn, T. Wimmer, J. Barker, G. E. W. Bauer, Z. Qiu, E. Saitoh, N. Vlietstra, S. Geprägs, R. Gross, H. Huebl, and S. T. B. Goennenwein, Non-local magnon transport in the compensated ferrimagnet GdIG, arXiv:1705.02871.

[43] K. Ganzhorn, J. Barker, R. Schlitz, B. A. Piot, K. Ollefs, F. Guillou, F. Wilhelm, A. Rogalev, M. Opel, M. Althammer, S. Geprägs, H. Huebl, R. Gross, G. E. W. Bauer, and S. T. B. Goennenwein, Spin Hall magnetoresistance in a canted ferrimagnet, Phys. Rev. B **94**, 094401 (2016).

[44] H. Maier-Flaig, S. Geprägs, Z. Qiu, E. Saitoh, R. Gross, M. Weiler, H. Huebl, and S. T. B. Goennenwein, Perpendicular magnetic anisotropy in insulating ferrimagnetic gadolinium iron garnet thin films, arXiv:1706.08488.

[45] S. Geprägs, A. Kehlberger, F. Della Coletta, Z. Qiu, E.-J. Guo, T. Schulz, C. Mix, S. Meyer, A. Kamra, M. Althammer, H. Huebl, G. Jakob, Y. Ohnuma, H. Adachi, J. Barker, S. Maekawa, G. E. W. Bauer, E. Saitoh, R. Gross, S. T. B. Goennenwein, and M. Kläui, Origin of the spin Seebeck effect in compensated ferrimagnets, Nat. Commun. **7**, 10452 (2016).

[46] C. Dubs, O. Surzhenko, R. Linke, A. Danilewsky, U. Brückner, and J. Dellith, Sub-micrometer yttrium iron garnet LPE films with low ferromagnetic resonance losses, J. Phys. D. Appl. Phys. **50**, 204005 (2017).

[47] S. A. Manuilov and A. M. Grishin, Pulsed laser deposited $Y_3Fe_5O_{12}$ films: Nature of magnetic anisotropy I, J. Appl. Phys. **108**, 123917 (2010).

[48] S. A. Manuilov and A. M. Grishin, Pulsed laser deposited $Y_3Fe_5O_{12}$ films: Nature of magnetic anisotropy II, J. Appl. Phys. **108**, 013902 (2010).

[49] C. Hauser, T. Richter, N. Homonnay, C. Eisenschmidt, M. Qaid, H. Deniz, D. Hesse, M. Sawicki, S. G. Ebbinghaus, and G. Schmidt, Yttrium iron garnet thin films with very low damping obtained by recrystallization of amorphous material, Sci. Rep. **6**, 20827 (2016).

[50] H. Chang, P. Li, W. Zhang, T. Liu, A. Hoffmann, L. Deng, and M. Wu, Nanometer-thick yttrium iron garnet films with extremely low damping, IEEE Magn. Lett. **5**, 6700104 (2014).

[51] E. L. Jakubisova, S. Visnovsky, H. Chang, and M. Wu, Interface effects in nanometer-thick yttrium iron garnet films studied by magneto-optical spectroscopy, Appl. Phys. Lett. **108**, 082403 (2016).

[52] A. Mitra, O. Cespedes, Q. Ramasse, M. Ali, S. Marmion, M. Ward, R. M. D. Brydson, C. J. Kinane, J. F. K. Cooper, S. Langridge, and B. J. Hickey, Interfacial origin of the magnetisation suppression of thin film yttrium iron garnet, Sci. Rep. **7**, 11774 (2017).

[53] J. C. Gallagher, A. S. Yang, J. T. Brangham, B. D. Esser, S. P. White, M. R. Page, K. Y. Meng, S. Yu, R. Adur, W. Ruane, S. R. Dunsiger, D. W. McComb, F. Yang, and P. C. Hammel, Exceptionally high magnetization of stoichiometric $Y_3Fe_5O_{12}$ epitaxial films grown on $Gd_3Ga_5O_{12}$, Appl. Phys. Lett. **109**, 072401 (2016).

[54] R. A. Duine, K.-J. Lee, S. S. P. Parkin, and M. D. Stiles, Synthetic antiferromagnetic spintronics, Nat. Phys. **14**, 217 (2018).

[55] K. W. Urban, C.-L. Jia, L. Houben, M. Lentzen, S.-B. Mi, and K. Tillmann, Negative spherical aberration ultrahigh-resolution imaging in corrected transmission electron microscopy, Philos. Trans. R. Soc. A Math. Phys. Eng. Sci. **367**, 3735 (2009).

[56] A. K. Gutakovskii, A. L. Chuvilin, and S. A. Song, Application of high-resolution electron microscopy for visualization and quantitative analysis of strain fields in heterostructures, Bull. Russ. Acad. Sci. Phys. **71**, 1426 (2007).

[57] E. Villamor, M. Isasa, L. E. Hueso, and F. Casanova, Temperature dependence of spin polarization in ferromagnetic metals using lateral spin valves, Phys. Rev. B **88**, 184411 (2013).

[58] E. Villamor, L. E. Hueso, and F. Casanova, Effect of the interface resistance in non-local Hanle measurements, J. Appl. Phys. **117**, 223911 (2015).

[59] L. Pietrobon, L. Fallarino, A. Berger, A. Chuvilin, F. Casanova, and L. E. Hueso, Weak delocalization in graphene on a ferromagnetic insulating film, Small **11**, 6295 (2015).

[60] A. Barla, J. Nicolás, D. Cocco, S. M. Valvidares, J. Herrero-Martín, P. Gargiani, J. Moldes, C. Ruget, E. Pellegrin, and S. Ferrer, Design and performance of BOREAS, the beamline for resonant X-ray absorption and scattering experiments at the ALBA synchrotron light source, J. Synchrotron Radiat. **23**, 1507 (2016).

[61] See Supplemental Material at http://link.aps.org/supplemental/10.1103/PhysRevApplied.10.044046, which includes Refs. [75-83], for further characterization of the samples.

[62] Values extracted from [ref. 63].

[63] S. Geller, G. P. Espinosa, and P. B. Crandall, Thermal expansion of yttrium and gadolinium iron, gallium and aluminum garnets, J. Appl. Crystallogr. **2**, 86 (1969).

[64] N. Thiery, V. V. Naletov, L. Vila, A. Marty, A. Brenac, J.-F. Jacquot, G. de Loubens, M. Viret, A. Anane, V. Cros, J. Ben Youssef, V. E. Demidov, S. O. Demokritov, and O. Klein, Electrical properties of single crystal yttrium iron garnet ultra-thin films at high temperatures, Phys. Rev. B **97**, 064422 (2018).

[65] C. Hahn, G. De Loubens, O. Klein, M. Viret, V. V. Naletov, and J. Ben Youssef, Comparative measurements of inverse spin Hall effects and magnetoresistance in YIG/Pt and YIG/Ta, Phys. Rev. B **87**, 174417 (2013).

[66] P. Wang, S. W. Jiang, Z. Z. Luan, L. F. Zhou, H. F. Ding, Y. Zhou, X. D. Tao, and D. Wu, Spin rectification induced by spin Hall magnetoresistance at room temperature, Appl. Phys. Lett. **109**, 112406 (2016).

[67] J. Chakhalian, J. W. Freeland, H. U. Habermeier, G. Cristiani, G. Khaliullin, M. Van Veenendaal, and B. Keimer, Orbital reconstruction and covalent bonding at an oxide interface, Science (80-.) **318**, 1114 (2007).

[68] G. F. Dionne, Molecular field coefficients of substituted yttrium iron garnets, J. Appl. Phys. **41**, 4874 (1970).

[69] T. D. C. Higgs, S. Bonetti, H. Ohldag, N. Banerjee, X. L. Wang, A. J. Rosenberg, Z. Cai, J. H. Zhao, K. A. Moler, and J. W. A. Robinson, Magnetic coupling at rare earth ferromagnet/transition metal ferromagnet interfaces: A comprehensive study of Gd/Ni, Sci. Rep. **6**, 30092 (2016).

[70] A. B. Harris, Spin-wave spectra of yttrium and gadolinium iron garnet, Phys. Rev. **132**, 2398 (1962).

[71] T. Yamagishi, J. Awaka, Y. Kawashima, M. Uemura, S. Ebisu, S. Chikazawa, and S. Nagata, Ferrimagnetic order in the mixed garnet (Y1-xGd x)$_3$Fe$_5$O$_{12}$, Philos. Mag. **85**, 1819 (2005).

[72] R. E. Camley, Surface spin reorientation in thin Gd films on Fe in an applied magnetic field, Phys. Rev. B **35**, 3608 (1987).

[73] S. Parkin, X. Jiang, C. Kaiser, A. Panchula, K. Roche, and M. Samant, Magnetically engineered spintronic sensors and memory, Proc. IEEE **91**, 661 (2003).

[74] T. Jungwirth, X. Marti, P. Wadley, and J. Wunderlich, Antiferromagnetic spintronics, Nat. Nanotechnol. **11**, 231 (2016).

[75] J. F. K. Cooper, C. J. Kinane, S. Langridge, M. Ali, B. J. Hickey, T. Niizeki, K. Uchida, E. Saitoh, H. Ambaye, and A. Glavic, Unexpected structural and magnetic depth dependence of YIG thin films, Phys. Rev. B **96**, 104404 (2017).

[76] C. Tang, P. Sellappan, Y. Liu, Y. Xu, J. E. Garay, and J. Shi, Anomalous Hall hysteresis in Tm$_3$Fe$_5$O$_{12}$/Pt with strain-induced perpendicular magnetic anisotropy, Phys. Rev. B **94**, 140403 (2016).

[77] M. Haidar, M. Ranjbar, M. Balinsky, R. K. Dumas, S. Khartsev, and J. Åkerman, Thickness- and temperature-dependent magnetodynamic properties of yttrium iron garnet thin films, J. Appl. Phys. **117**, 17D119 (2015).

[78] N. S. Sokolov, V. V. Fedorov, A. M. Korovin, S. M. Suturin, D. A. Baranov, S. V. Gastev, B. B. Krichevtsov, K. Y. Maksimova, A. I. Grunin, V. E. Bursian, L. V. Lutsev, and M. Tabuchi, Thin yttrium iron garnet films grown by pulsed laser deposition: Crystal structure, static, and dynamic magnetic properties, J. Appl. Phys. **119**, 023903 (2016).

[79] L. McKenzie-Sell, M. Amado, G. Kimbell, G. Divitini, C. Ciccarelli, and J. W. A. Robinson, Low-temperature ferromagnetic resonance in yttrium iron garnet thin films: role of substrate-induced impurities, to be submitted (n.d.).

[80] C. Kittel, Introduction to Solid State Physics, *Introduction to Solid State Physics*, 8th ed. (Wiley, 2004).

[81] C. L. Jermain, S. V. Aradhya, N. D. Reynolds, R. A. Buhrman, J. T. Brangham, M. R. Page, P. C. Hammel, F. Y. Yang, and D. C. Ralph, Increased low-temperature damping in yttrium iron garnet thin films, Phys. Rev. B **95**, 174411 (2017).

[82] S. B. Ubizskii, Orientational states of magnetization in epitaxial (111)-oriented iron garnet films, J. Magn. Magn. Mater. **195**, 575 (1999).